
WEIGHING THE GIANTS USING COSMIC MICROWAVE BACKGROUND LENSING

SANJAYKUMAR PATIL
Doctor of Philosophy

SCHOOL OF PHYSICS
THE UNIVERSITY OF MELBOURNE

*Submitted in Total Fulfillment of the
Requirements of the Degree of Doctor of Philosophy*

Statement of contribution:

This is to certify that:

- This thesis entitled TITLE the thesis comprises only their original work towards the degree of Doctor of Philosophy.
- Due acknowledgement has been made in the text to all other material used.
- The thesis is less than 100,000 words in length, exclusive of tables, maps, bibliographies, and appendices.

Contents

Chapter 1: Introduction	1
Chapter 2: Data	3
Chapter 3: modified Quadratic Estimator	5
3.1 Thermal Sunayev-Zel'dovich effect	5
3.2 Methods	7
3.3 Quadratic Estimator	7
3.3.1 mitigating magnification bias	9
3.4 modifications of Quadratic Estimator	10
3.4.1 modified Quadratic Estimator	10
3.5 Data	11
3.6 South Pole Telescope	11
3.6.1 SPTpol 500 deg ² survey	11
3.6.2 DES and the redMaPPer catalog	12
3.6.3 fitting model	13
3.7 cluster cutouts and weighing scheme	14
3.8 Results and Discussion	15
3.8.1 Stacked mass measurements	16
3.8.2 Mass-richness $M - \lambda$ scaling relation calibration	17
Chapter 4: Template Fitting	19
4.1 Method	19
4.1.1 Template fitting to reduce the SZ variance	20
4.2 Results	24
4.2.1 Sources of uncertainty in the CMB-Cluster Lensing Measurement	24
4.3 Results	25
4.3.1 Performance comparision	26
4.3.2 Robustness of template fitting method	26
4.3.3 Miscentering	27

4.4 Forecasts	28
Appendix A:Appendix A	31
A.1 Section in an appendix	31

List of Tables

List of Figures

3.1	The plot shows the intensity of CMB as function of frequency before (black) and after (blue) it passes through a cluster.	6
3.2	Galaxy cluster of mass $M_{200m} = 5 * 10^{14} M_{\odot}$ as seen in a CMB survey with following specifications : 1.'7 beam at 90 GHz (left panel) and 1'beam at 150 GHz (right panel).	7
3.3	Effect of SZ on lensing convergence profile. On the top panel we show the lensing convergence profile for a stack of 1000 cluster each at a mass of $M_{200m} = 2 * 10^{14} M_{\odot}$ and a redshift of $z = 0.7$ with experimental white noise level of $3\mu K - \text{arcmin}$; left panel is without SZ and right panel is with SZ. On the bottom panel we have radial profile of the same in solid blue (without SZ) and green (with SZ) curves; black curve is the radial profile of the input NFW profile.	8
3.4	Gradient of temperature field as a function of low pass filter $l = l_G$. It is dominated by multipoles below 2000. check the magnitude of Grms . . .	10
3.5	Gradient of temperature field as a function of low pass filter $l = l_G$. It is dominated by multipoles below 2000. check the magnitude of Grms . . .	15
3.6	It shows	16
3.7	It shows	17
3.8	It shows	18
4.1	explain why no bias	21

4.2	Template fitting significantly reduces SZ power, even with an imperfect match between the template and true SZ signal. The top left panel (a) shows the expected Arnaud profile for a galaxy cluster of mass $M_{200m} = 510^{14} M_{\odot}$ at $z=0.7$ after being smoothed by Gaussian beam with FWHM= $1'.7$. The top right panel (b) shows the residuals after subtracting the best-fit $2'.0$ FWHM Gaussian (the amplitude is free, but the FWHM is fixed). The lower panel (c) shows one-dimensional slices through each panel: the solid, blue line is a slice through the beam-convolved Arnaud profile of (a), and the dashed green line is a slice through the residual map in (b).	23
4.3	Ratio of SZ variance over kappa variance as a function of cluster mass and experimental noise level. As expected the ratio increases with mass for a given experimental noise level. The black solid line represents the points where the ratio SZ variance is equal to that of experimental noise.	24
4.4	Projecting out an SZ template from the second leg of the modified QE improves the performance for all masses considered. Here we show the percentage mass uncertainties from three methods for a sample of 1000 clusters at a experimental noise level of $3 \mu\text{K-arcmin}$. All the curves use an SZ-free map for the gradient, but make different assumptions about the second, high-pass filtered map. [SR: Replace “mQE” to w/o template fitting. They are all mQE. Change xlabel to M_{200m} . Change line styles to match text].	27
4.5	Our new method is robust to realistic SZ simulations. The red and black solid curves show the performance of modified QE for the Sehgal and Takahashi simulations respectively. The dashed lines show the improvement in each case when template fitting is used to reduce the SZ variance in the small-scale map. [SR: Change xlabel to M_{200m}].	28
4.6	Our new method is robust to realistic SZ simulations. The red and black solid curves show the performance of modified QE for the Sehgal and Takahashi simulations respectively. The dashed lines show the improvement in each case when template fitting is used to reduce the SZ variance in the small-scale map. [SR: Change xlabel to M_{200m}].	29

Chapter 1

Introduction

Expanding Universe

- Explain cosmological principle and hubble's law
- FLRW metric, $a(t)$ at various epochs in the universe
- Ending with supernovae and dark energy

CMB

- Epoch of recombination
- CMB power spectrum
- CMB secondary anisotropies (introduce tSZ and CMB lensing)

Λ CDM cosmology

- Explain different cosmological parameters and probes

Galaxy Clusters

- Introduction to galaxy clusters
- Clusters as Cosmological Probes
- Difficulty with mass estimation
- Measuring mass of Galaxy clusters using CMB lensing.

Chapter 2

Data_____

Chapter 3

modified Quadratic Estimator

Overview

In this chapter we discuss modified Quadratic Estimator which we have developed to eliminate the bias due thermal Sunyaev Zel'dovich (SZ) effect. We give a brief review thermal Sunayev-Zel'dovich effect (refer [citations](#) for a detailed review) and its effect on cluster lensing in the §3.1. Then we discuss the modifications of the QE to remove SZ bias in §3.2. Later we explain the SPTpol and DES data sets in §3.5 and results in §4.3 Finally we conclude in §??.

3.1 Thermal Sunayev-Zel'dovich effect

Cosmic microwave background (CMB) photons gets inverse Thompson scattered off the high energetic electrons present in the intra cluster medium of a galaxy cluster, resulting in a deficiency of photons at lower frequency and excess of photons at higher frequency. This phenomena is called thermal Sunayev-Zel'dovich effect (SZ). SZ is a small effect and to illustrate it we have shown CMB spectral distortion for a fictional galaxy cluster of mass 1000 times more that of a typical galaxy cluster in Fig 3.1. The solid black curve represents the intensity of CMB as a function of frequency before its interaction with hot intracluster medium; solid blue represents the same after its interaction. As shown in the Fig. 3.1, SZ decreases the intensity of CMB below a frequency of 220 GHz and increases at higher frequencies.

The fractional change in temperature is given by

$$\frac{\Delta T_{SZ}}{T_{CMB}} = f(x)y = f(x) \int n_e \frac{k_B T_e}{m_e c^2} \sigma_T dl \quad (3.1)$$

where y is Compton y -parameter, n_e is the electron number density, m_e is the electron rest mass, c is the speed of light, T_e is the electron temperature, σ_T is the Thompson cross-section, and $f(x)$ is the dimensionless frequency given by

$$f(x) = \left(x \frac{e^x + 1}{e^x - 1} - 4\right)(1 + \delta_{SZE}(x, T_e)) \quad (3.2)$$

where $\delta_{SZE}(x, T_e)$ is the relativistic correction to the frequency dependence.

As can be seen in 3.1 SZ effect is independent of redshift and has potential to

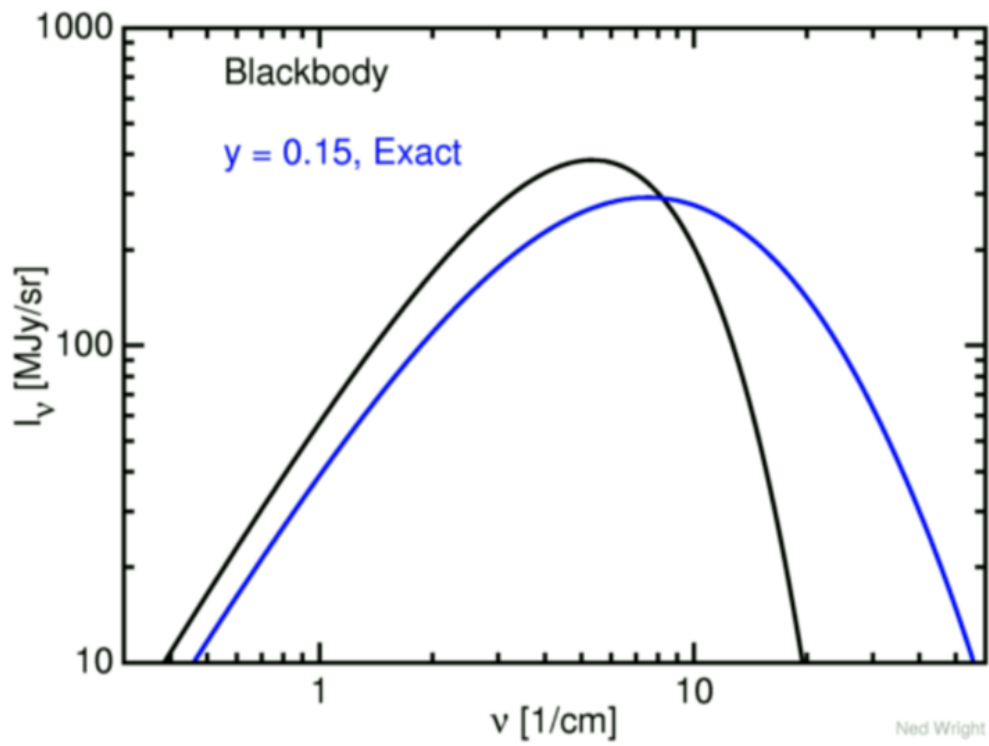


Figure 3.1: The plot shows the intensity of CMB as function of frequency before (black) and after (blue) it passes through a cluster.

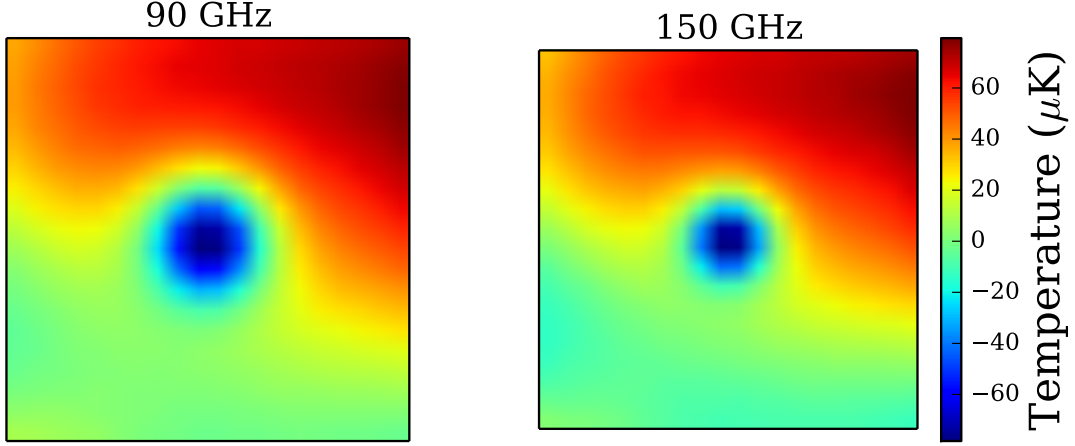


Figure 3.2: Galaxy cluster of mass $M_{200m} = 5 \times 10^{14} M_{\odot}$ as seen in a CMB survey with following specifications : $1.7'$ beam at 90 GHz (left panel) and $1'$ beam at 150 GHz (right panel).

high redshift clusters, where the cluster abundance critically depends on underlying Cosmology. CMB surveys use SZ effect to detect galaxy clusters; Fig. 3.1 shows a galaxy cluster of mass $M_{200m}^1 = 5 \times 10^{14} M_{\odot}$ as seen by CMB survey.

Though SZ is small spectral effect, it is still much higher than the lensing signal. It is an order of magnitude greater than the lensing signal and hence induces a significant systematic and statistical uncertainty if not taken into account. Fig. 3.3 shows the effect of SZ on the lensing convergence profile. In the left panel of figure we show the stacked lensing convergence profile of 1000 clusters each with a mass of $4 \times 10^{14} M_{\odot}$ and an experimental noise of $1 \mu K'$ with no SZ and on the right panel is with the SZ. As can be inferred from the plot, presence of SZ induces a blue blob in the center and hence resulting in a negative bias.

3.2 Methods

3.3 Quadratic Estimator

Typical size of galaxy cluster is of the order of few arc minutes. Primordial CMB doesn't have power at such small scales due to diffusion damping[?] and can be approximated as a gradient. Lensing due to galaxy cluster induces a dipole kind of structure oriented along the direction of background gradient with hot and cold spots swapped. For a given cluster mass and redshift, the magnitude of this dipole scales linearly with the magnitude of the CMB gradient. This correlation between the unlensed CMB gradient

¹ M_{200m} is defined as the mass of the cluster within a radius R_{200} , within which the cluster density is 200 times the critical density of the Universe at cluster redshift

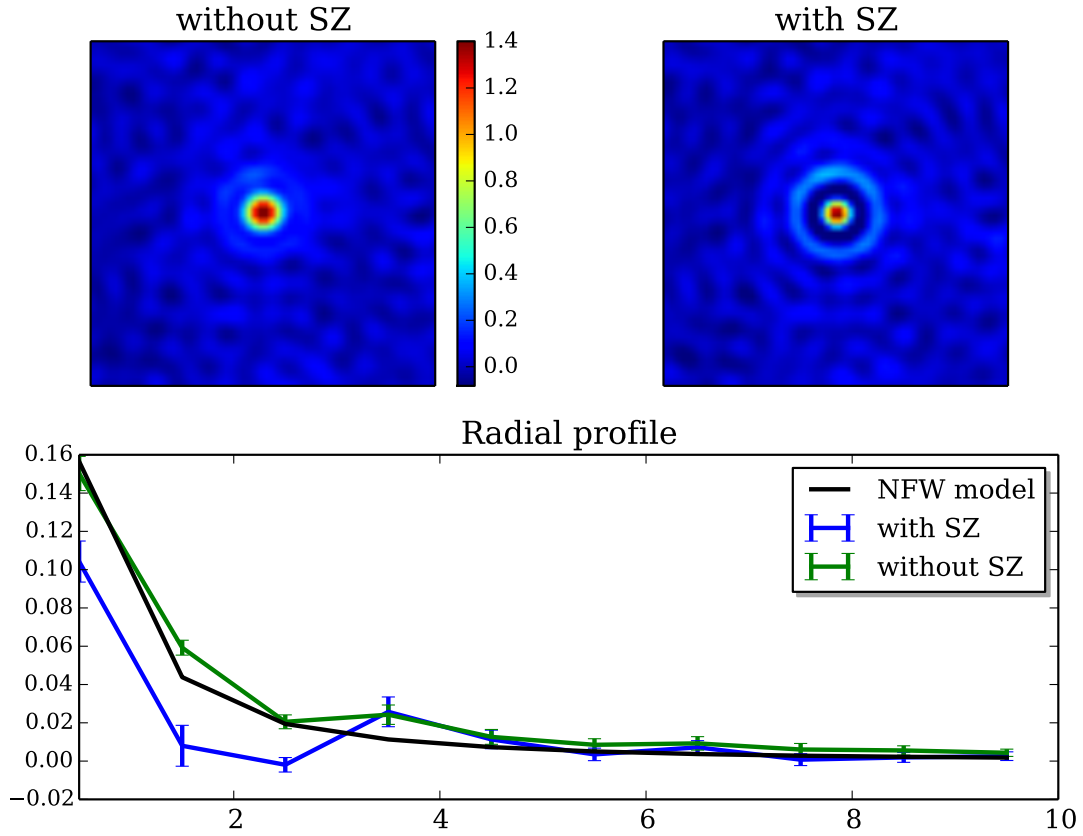


Figure 3.3: Effect of SZ on lensing convergence profile. On the top panel we show the lensing convergence profile for a stack of 1000 cluster each at a mass of $M_{200m} = 2 \times 10^{14} M_{\odot}$ and a redshift of $z = 0.7$ with experimental white noise level of $3\mu\text{K} - \text{arcmin}$; left panel is without SZ and right panel is with SZ. On the bottom panel we have radial profile of the same in solid blue (without SZ) and green (with SZ) curves; black curve is the radial profile of the input NFW profile.

and lensing signal is known as the gradient approximation and is equivalent to

$$T(\hat{n}) \approx \tilde{T} + \nabla T \cdot \tilde{\alpha}(\hat{n}) \quad (3.3)$$

Below we provide the mathematical formalism for temperature quadratic estimator and it generalises for polarisation.

Under the gradient approximation, we construct an estimator of lensing convergence by multiplying the lensing map and the gradient map. The gradient approximation doesn't hold for all Fourier modes, only for the modes which are correlated by reconstruction. We filter maps in the Fourier space to isolate modes for which the gradient approximation is valid. We obtain gradient and lensing maps as follows,

$$L(\hat{n}) = \int \frac{d^2 l}{(2\pi)^2} e^{il \cdot \hat{n}} W_l^T T_l \quad (3.4)$$

$$G(\hat{n}) = \nabla \left(\int \frac{d^2 l}{(2\pi)^2} e^{il \cdot \hat{n}} W_l^{TT} T_l \right) \quad (3.5)$$

where $G(\hat{n})$, $L(\hat{n})$ are filtered gradient and lensing maps and T_l is the observed temperature map in Fourier space. Fourier filters W_l^T and W_l^{TT} are given by

$$W_l^T = (C_l^{TT} + N_l^{TT})^{-1} \quad (3.6)$$

$$W_l^{TT} = \tilde{C}_l^{TT} (C_l^{TT} + N_l^{TT})^{-1} \quad (3.7)$$

where $\tilde{C}_l^{TT}, C_l^{TT}$ is the unlensed and large scale structure lensed CMB power spectrum obtained from CAMB, N_l^{TT} is the experimental noise power spectrum. With filtered gradient and lensing maps in hand we can write down the expression for lensing convergence profile as

$$\hat{k}_l = -A_l \int d^2 \hat{n} e^{i\hat{n} \cdot l} \text{Re} \nabla \cdot [G(\hat{n}) L^*(\hat{n})] \quad (3.8)$$

where A_l is the normalisation parameter given by

$$\frac{1}{A_l} = \frac{2}{l^2} \int \frac{d^2 l_1}{4\pi^2} (l \cdot l_1) W_l^{TT} W_{l_1}^T (\tilde{C}_{l_1}^{TT}(l \cdot l_1) + \tilde{C}_{l_2}^{TT}(l \cdot l_2)) \quad (3.9)$$

where $l = l_1 + l_2$.

3.3.1 mitigating magnification bias

Galaxy cluster magnifies the background image and decreases the observed temperature gradient behind it, which leads to a low bias in lensing reconstruction. The bias is due to the overlap in scales between the unlensed temperature gradient and the lensed temperature field. Though wiener filter reduces the bias, it is not removed completely. We can reduce the bias further by exploiting the prior knowledge on unlensed CMB

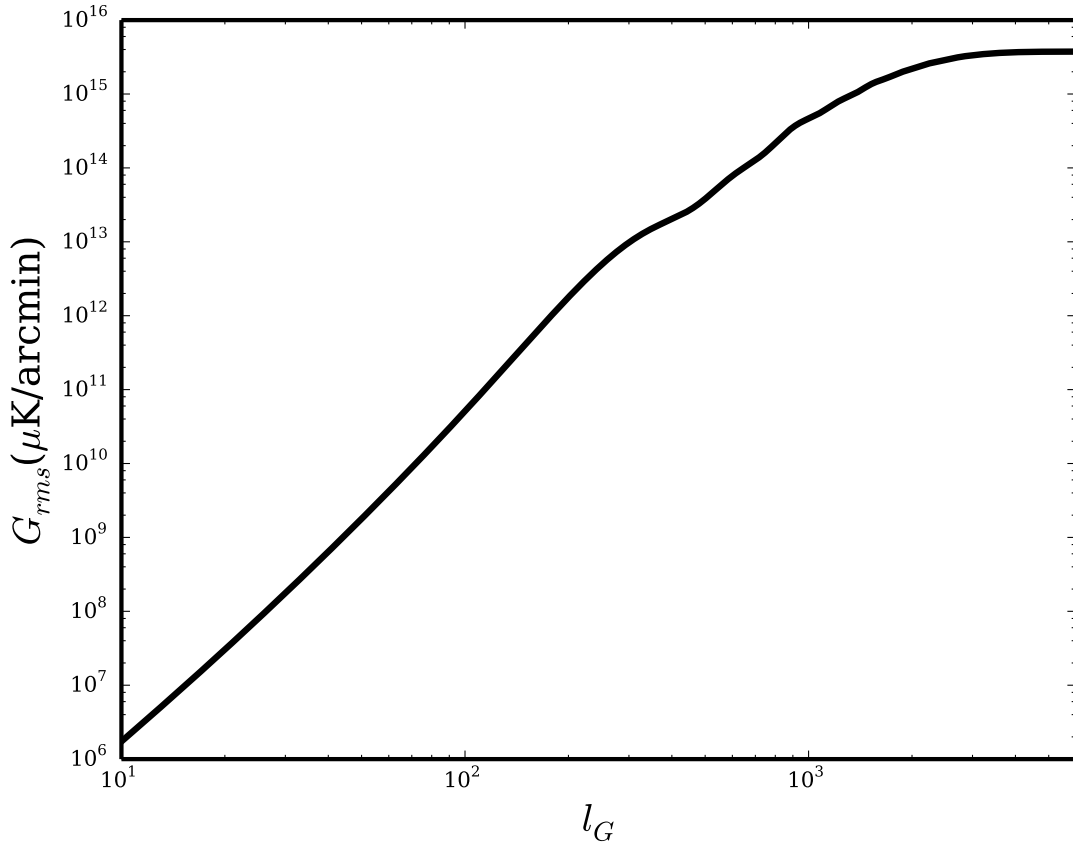


Figure 3.4: Gradient of temperature field as a function of low pass filter $l = l_G$. It is dominated by multipoles below 2000. check the magnitude of Grms

power spectrum. From Fig. 3.5, which shows the unlensed rms gradient as a function of multipoles, it is evident that most of the power for the gradient map comes from scales below $l < 2000$. By low pass filtering the gradient map, we separate the unlensed temperature gradient and the lensed temperature field with almost no loss in SNR.

3.4 modifications of Quadratic Estimator

The major foreground in CMB cluster lensing analysis is thermal Sunyaev -Zel'dovich (tSZ) effect. tSZ effect is an order of magnitude greater than lensing signal; if not taken into consideration it induces systematic bias and variance in the final convergence maps. In this section we describe the modifications of Quadratic Estimator to make it robust to both tSZ induced bias and variance.

3.4.1 modified Quadratic Estimator

While designed to pull the lensing induced correlations, QE is equally sensitive to any other signal present in both G and L maps. tSZ present in both maps results in a low bias. One way to eliminate tSZ bias is using tSZ free maps, which are constructed by

exploiting the frequency dependence of tSZ signal. However, this results in a increased statistical uncertainty in the reconstructed convergence profile. Another way to mitigate the bias is by using a more stringent low pass filter on the gradient map. By having a more robust separation of scales between gradient map and small scale map. While this can reduce the bias significantly, this results in a poor gradient estimation and hence increasing the statistically uncertainty.

During my thesis we came up with a novel approach to completely remove the tSZ bias. Any foreground signal which is present in both the maps will lead to a systematic bias, so by getting rid of the foreground signal in one of the maps (either G or L) should eliminate the bias completely. As shown in Fig. 3.5, most of the gradient estimation comes from multipoles $l < 2000$ and CMB is not limited by noise at those scales. So, natural choice would be to eliminate tSZ in the gradient map by using linear combination of different frequencies. In modified Quadratic Estimator, eqn 3.6 becomes,

$$G(\hat{n}) = \nabla \left(\int \frac{d^2l}{(2\pi)^2} e^{il \cdot \hat{n}} W_l^{TT} T_l^{SZ_{free}} \right) \quad (3.10)$$

where $T_l^{SZ_{free}}$ is the tSZ-free map.

3.5 Data

We use data sets from two different experiments: CMB maps from South Pole Telescope is explained in §3.6 and optical cluster catalog from Dark Energy Survey is explained in §3.6.2

3.6 South Pole Telescope

South Pole Telescope (SPT) is a 10 meter diameter, wide field, offset Gregorian telescope (SPT, ??) located at the Amundsen-Scott South Pole station. The SPT has been operating since early 2007 and has completed two surveys so far: SPT-SZ (2007 -2011) and SPTpol (2012-2016). Extremely dry and stable atmosphere of the south pole makes it one of the best available sites on Earth for observing millimeter and sub-millimeter wavelengths.

3.6.1 SPTpol 500 deg^2 survey

SPTpol is the second camera installed on the 10-meter South Pole Telescope (SPT, ??) located at the Amundsen-Scott South Pole station. The SPTpol focal plane consists of 1536 polarization-sensitive transition edge sensor bolometers (360 at 95 GHz and 1176 at 150 GHz) (?). The SPTpol 500 deg^2 survey spans fifteen degrees of declination, from -65 to -50 degrees, and four hours of right ascension, from 22h to 2h. In this work, we use CMB temperature maps from observations between April 2013 and September 2016 in frequency bands centered at approximately 95 GHz and 150 GHz. The telescope

beam and pointing solutions were characterized using Venus and bright point sources in the SPTpol survey region. The final telescope beam along with the pointing jitter roughly corresponds to a $\theta_{\text{FWHM}} = 1.''22$ ($1.''7$) Gaussian for the 150 (95) GHz dataset.

We briefly summarize the procedure we use to reduce raw CMB data to maps and refer the reader to ? for further details. The raw data are composed of digitized time-ordered data (TOD) for each detector that are converted into CMB temperature units. We bin the TOD into two different maps using a flat-sky approximation in the Sanson-Flamsteed projection (??). To construct the first map, in which we aim to reconstruct the small-scale lensing signal, we remove large-scale modes $\ell \leq 300$, bandpass filter the TOD in the range of approximately $300 \leq \ell_x \leq 20,000$, and bin them into $0.''5$ square pixels. For the second map, intended for estimation of the large-scale CMB gradient, we apply minimal TOD filtering by only removing modes below $\ell_x \leq 30$, and bin them into $3''$ square pixels. While we only use the data from the 150 GHz channel for the first map, the latter is a tSZ signal cleaned map produced by linearly combining the 95 and 150 GHz channels. We use this tSZ-free map to reconstruct the background gradient of the CMB at the cluster locations. As we will see later in §??, the gradient estimation using the tSZ-free map helps in removing the tSZ-induced lensing bias. The minimal filtering on this map allows us to recover large-scale modes which indeed helps in a better estimation of the background gradient. The $0.''5$ resolution 150 GHz map has a white noise level of $\Delta_{\text{T}} = 6 \mu\text{K}'$ estimated using a jackknife approach. The low-resolution tSZ-free combination is noisier with $\Delta_{\text{T}} \sim 17 \mu\text{K}'$. **Noise power spectrum plot**

3.6.2 DES and the redMaPPer catalog

The Dark Energy Survey (DES) was a $\sim 5000 \text{ deg}^2$, optical to near-infrared survey conducted using the Dark Energy Camera (?) mounted on the 4-meter Victor Blanco telescope at Cerro Tololo Observatory in Chile and has recently finished its survey. For this analysis, we use the cluster catalog obtained from the first three years of DES observations, which almost covers the SPTpol 500 deg^2 survey.

The cluster catalog was derived using the RM algorithm (?). RM is an optical cluster-finding algorithm which detects candidates by identifying over-densities of luminous red galaxies with luminosity greater than 20% of L_* . It is based on our understanding that galaxy clusters are agglomerations of galaxies containing old and subsequently red stars. The algorithm iteratively assigns membership and centering probabilities for each red galaxy identified as belonging to a cluster candidate. A weighted sum of the membership probabilities, richness λ , is assigned to each candidate. The centre comes from the galaxy with the highest centering probability. The DES RM catalog contains two samples: a flux-limited sample and a volume-limited sample. The flux-limited sample has more high-redshift clusters detected from deep fields in the survey. On the other

hand, the volume-limited sample is independent of survey depth, complete above a luminosity threshold (?, hereafter ?), and normally preferred for cosmological analysis. See ? for more information on the application of RM to the DES survey data.

The RM cluster catalog version employed in this analysis is `y3_gold:v6.4.22`. The Year-3 gold catalogue is based on the previous catalog from the Year-1 data (?) with some updates described in ?. The catalog contains 54,112 clusters above richness $\lambda \geq 20$ in the flux-limited sample and 21,094 clusters in the volume-limited sample. Of these, 5,828 (2,428) clusters from the flux(volume)-limited sample lie within the SPTpol 500 deg² survey in the redshift range $0.1 \leq z \leq 0.95$ (0.90). We additionally remove clusters near the survey edges by removing the cutouts (see ??) with more than 5% masked pixels or within 10' distance from any bright (≥ 6 mJy at 150 GHz) point sources detected in the SPTpol temperature map. These cuts leave 4,003 (1,741) clusters with $\lambda \geq 20$ from the flux(volume)-limited sample with a median redshift of $\tilde{z} = 0.77$ (0.48). The error in the cluster photo- z estimates are small with $\hat{\sigma}_z = 0.01(1+z)$ (?). **include a figure with SPTpol map and pointing to a cluster**

3.6.3 fitting model

To obtain the mass of the cluster, we need to compare the observed lensing profile to the convergence model generated using an assumed halo mass profile. The observed lensing convergence profile of cluster has contributions from its own halo density (k_{1h}) as well as from the correlated structures along the line of sight known as two halo term (k_{2h}). For k_{1h} , we assume the galaxy cluster density to follow Navarro Frenk White (NFW) profile and in ?? we quantify the robustness of this assumption by using Einasto profile (?). A NFW halo profile is characterized by its scale radius R_s , the dimensionless concentration parameter c , and the dimensionless characteristic over-density δ_c . The characteristic over density is defined as the ratio central cluster density to the critical density of the Universe at the cluster redshift. In terms of these quantities the NFW halo density profile is written as

$$\rho(r) = \frac{\delta_c \rho_{crit,z}}{\left(\frac{r}{R_s}\right)\left(1 + \frac{r}{R_s}\right)^2} \quad (3.11)$$

where $\rho_{crit,z}$ is the critical density of the Universe at cluster redshift.

The lensing convergence profile is the ratio of surface mass density to the critical surface density of the Universe at cluster redshift, $k(x) = \frac{\Sigma(x)}{\Sigma_{crit}}$, where

$$\Sigma(x) = 2 \int_0^{\inf} \rho(r) ds \quad (3.12)$$

$$\Sigma(crit) = \frac{c^2}{4\pi G} \frac{D_{CMB}}{D_{clus} D_{CMB,clus}} \quad (3.13)$$

Here r is the distance from the center, x is the corresponding projection on the plane, D_{CMB} and D_{clus} are the comoving distances to the CMB and galaxy cluster respectively; $D_{CMB,clus}$ is the distance between the CMB and the cluster.

We model the two halo term, k_{2h} , by using the Eq. 13 of [Oguri and Hamana](#). With model prediction in hand we can write down the likelihood of observing the data as:

$$-2\ln L(k|M) = (k - k_m)(M)C^{-1}[(k - k_m)]^T \quad (3.14)$$

where k is the observed lensing convergence profile, k_m is lensing convergence for NFW profile at mass M , and C is the covariance matrix. Note that the contribution from the two halo term is considered only for real and not the pipeline verification in §??

3.7 cluster cutouts and weighing scheme

We extract 300'square box form SPTpol temperature maps at the DES cluster locations. While the boxsize is much larger than the virial radius of the cluster, it is necessary to robustly approximate the background gradient. This is because much of the gradient power comes from larger scale modes, reducing the analysis to a smaller box will reduce the SNR of the mass estimation. These cutouts are then passed through the pipeline to extract lensing convergence profile. After extracting the convergence profile, we limit modelling and likelihood calculations to 10'box around a cluster.

As mentioned before, the lensing signal is weak for individual cluster and we need to stack lensing convergence profiles to increase the SNR of detection. While

The schematic representation of Quadratic Estimator is shown in Fig 2. Panel (a) is the 10'X 10'cutout of the observed temperature map, T_l . This is filtered in the fourier space [mention equations](#) to obtain the filtered gradient and lensing maps, shown in panel (b) and (c) respectively. Lensing convergence profile (panel (c)) is reconstructed by extracting the correlations between lensing and gradient maps.

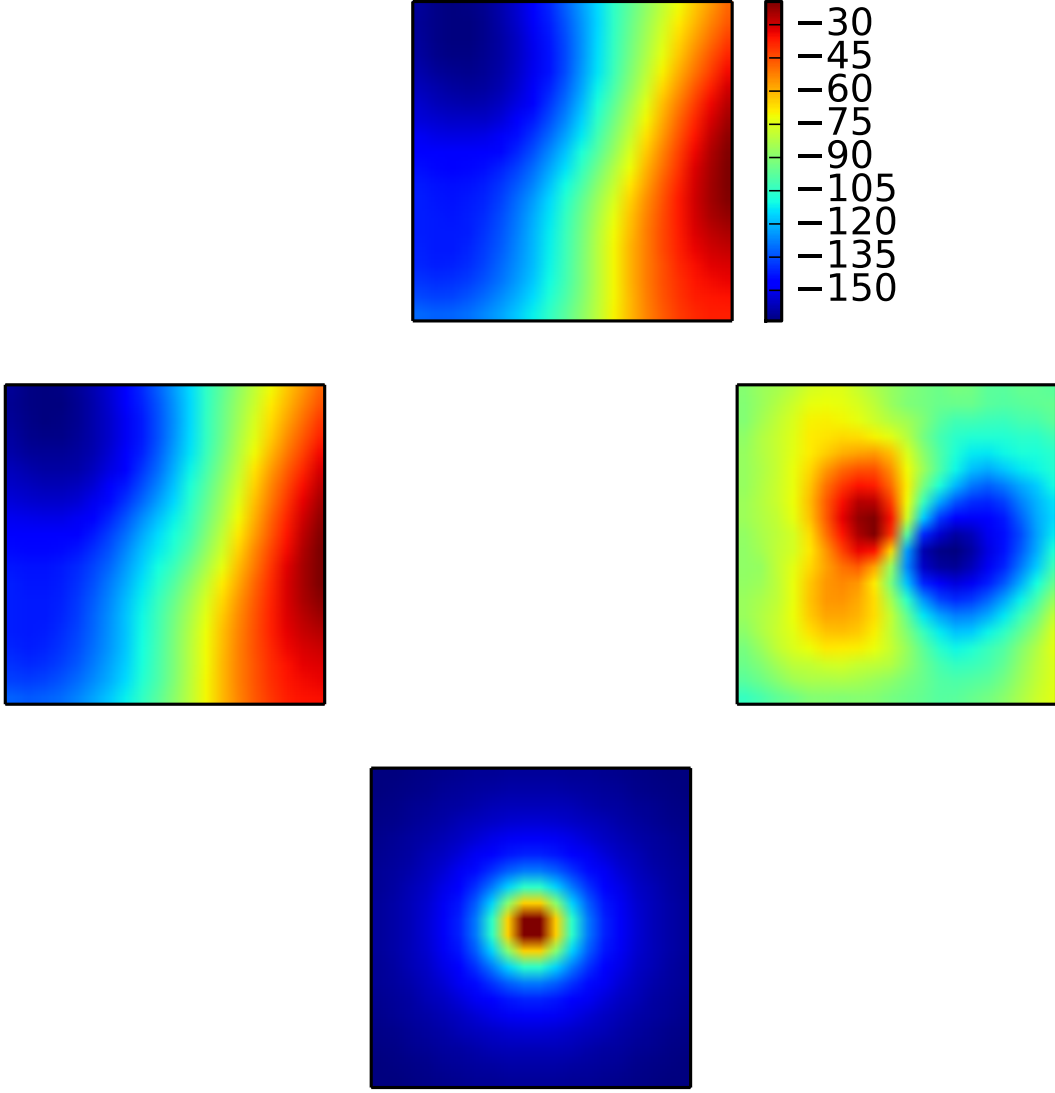


Figure 3.5: Gradient of temperature field as a function of low pass filter $l = l_G$. It is dominated by multipoles below 2000. *check the magnitude of Grms*

3.8 Results and Discussion

The main results of this work are the lensing-derived cluster mass constraints for the DES RM Year-3 cluster samples using SPTpol tSZ-free $\times 150$ GHz temperature maps. Below, we first present the lensing mass estimates in §3.8.1 and use the lensing measurements from the DES Year-3 volume-limited sample to independently calibrate the $M - \lambda$ relation of the cluster sample in

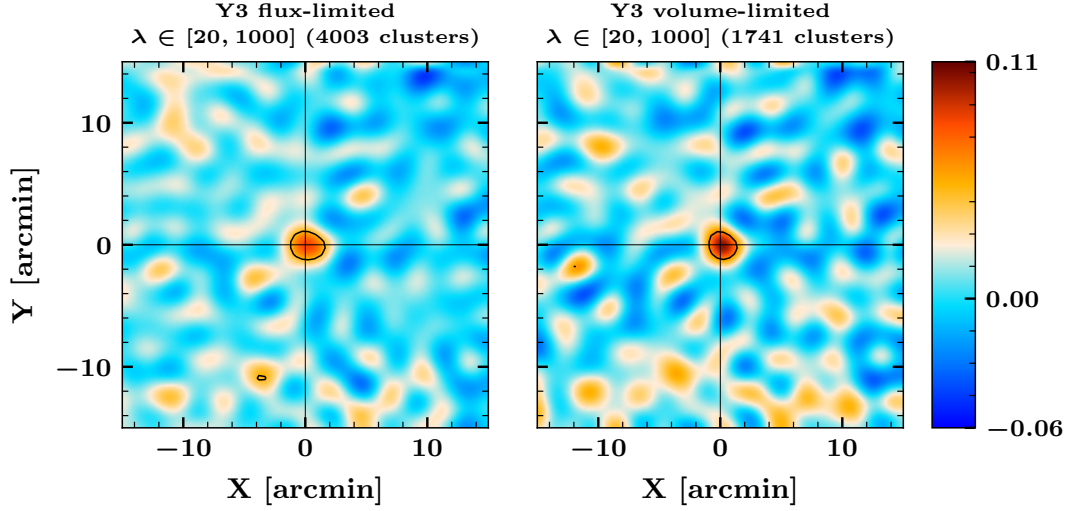


Figure 3.6: It shows

3.8.1 Stacked mass measurements

In Fig. ??, we present the results of our stacked lensing measurements. The left (right) panel correspond to the convergence maps stacked at the location of clusters in the DES Year-3 flux(volume)-limited sample. The variance in the flux-limited sample is lower than the volume-limited sample because the flux-limited sample has twice as many objects. An estimate of the mean-field has been subtracted from the maps. We reject the null hypothesis of no lensing with a significance of 8.7σ for the flux-limited sample of 4003 clusters. The obtained S/N is consistent with our expectations from the simulations shown as lighter black circles in For the smaller volume-limited sample, the no-lensing hypothesis is ruled out at 6.7σ . The radially binned convergence profiles that are used to estimate the cluster masses are shown in Fig. ?? along with the best-fit model curves.

The ringing pattern is because of the sharp filtering of modes above the SPTpol beam scale. The error bars plotted are the square root of the diagonal entries of the covariance matrix estimated using The recovered lensing masses for the stacked flux and volume-limited samples are According to expectations, the lensing masses shift up by 0.3σ when the *2-halo* term is excluded.

A higher mean mass is expected for the volume-limited sample. At redshifts above $z \sim 0.6$, galaxies at the luminosity threshold adopted by RM become too faint to be detected in the DES data. Consequently, the richness of the clusters is extrapolated from the subset of galaxies that are sufficiently bright to be detected. This extrapolation introduces additional noise in the richness estimates. The increased scatter leads to more low-mass systems scattering up to apparently rich systems, thereby lowering the mean

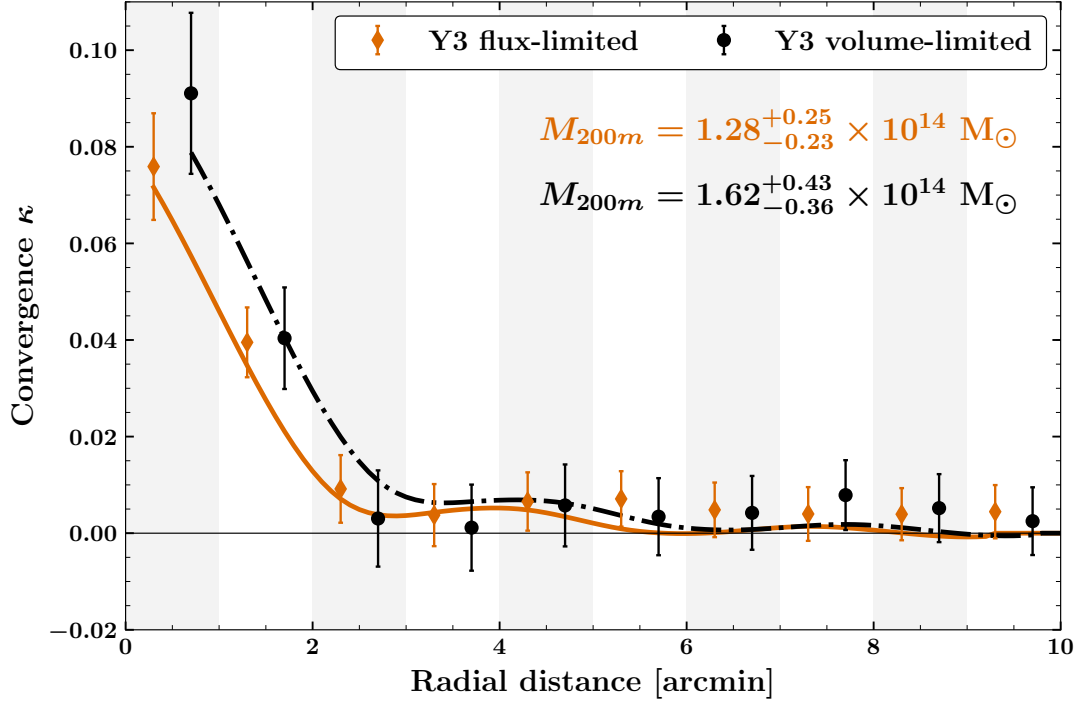


Figure 3.7: It shows

mass of the selected halos. For this reason, we restrict our analysis to the volume-limited sample in the subsequent sections.

3.8.2 Mass-richness $M - \lambda$ scaling relation calibration

We now apply the lensing mass measurements from §3.8.1 to constrain the relationship between a cluster's mass, M , and optical richness, λ , in the DES RM Year-3 volume-limited sample. We limit the analysis to just the volume-limited sample since the flux-limited sample has selection bias as explained above in §3.8.1. Following earlier weak-lensing analyses of RM clusters (???), we use a power-law scaling relation for cluster mass, M , as a function of richness, λ , and redshift, z ,

$$M = A \left(\frac{\lambda}{40} \right)^{\alpha} \left(\frac{1+z}{1+0.35} \right)^{\beta}, \quad (3.15)$$

where A is a normalization parameter, and the exponents α and β are richness and redshift evolution parameters respectively. The pivot points for the richness and redshift evolution were set based on DES weak-lensing measurements of ?. The model for the stacked mass is

$$M(A, \alpha, \beta) \equiv M = \frac{\sum_j w_j M(\lambda_j, z_j)}{\sum_j w_j}, \quad (3.16)$$

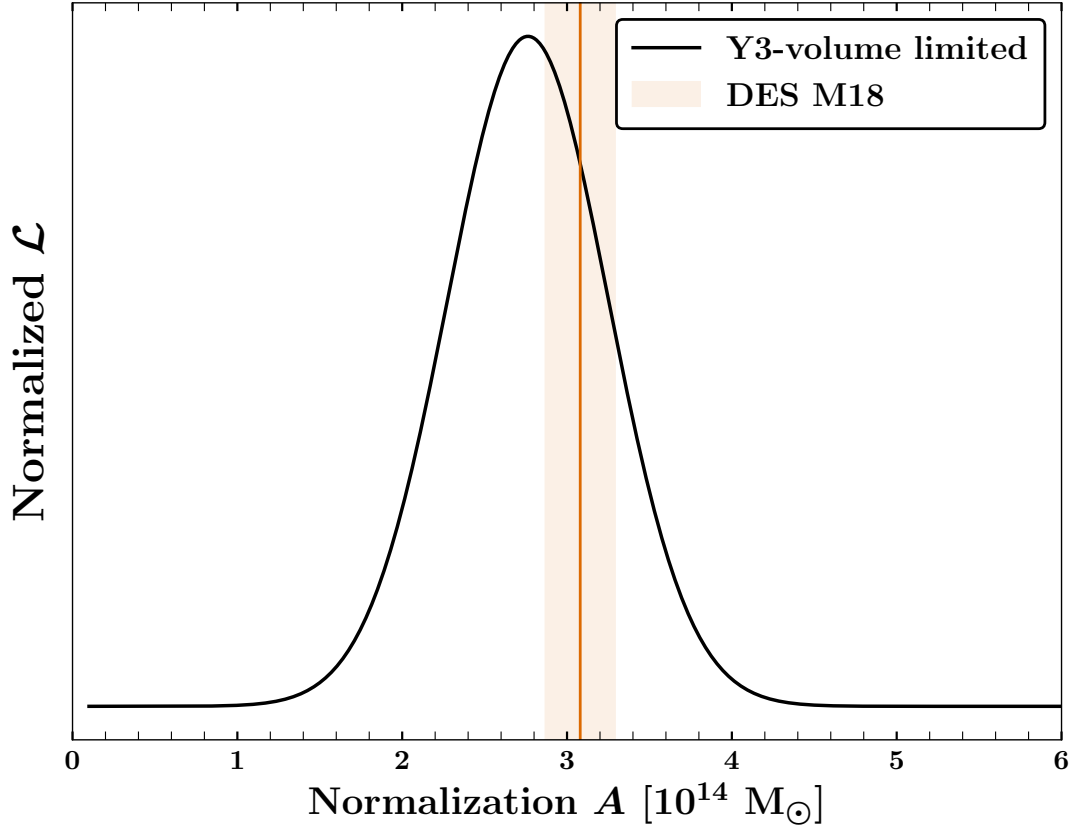


Figure 3.8: It shows

where the sum runs over the number of clusters in the sample and the weight w for each cluster is given in Eq. (??).

We do not split the stacks into different richness or redshift bins. As a result, the data's sensitivity to the two evolution parameters is minimal and we apply informative priors to both. We perform a Markov chain Monte Carlo (MCMC) analysis using the publicly available *emcee* (?) code to sample the likelihood space.

Chapter 4

Template Fitting

Modified Quadratic Estimator (mQE) developed in the last chapter completely eliminates the thermal Sunyaev-Zel'dovich (SZ) bias by using a SZ free gradient map. Though SZ bias is removed in mQE, SZ present in the second leg induces extra variance in the reconstructed lensing convergence profile. Unlike the variance due to other sources such as instrumental noise, uncorrelated foregrounds etc., SZ variance depends on the mass of galaxy cluster. SZ variance scales roughly with the mass of cluster as $M^{5/3}$. For DES X SPTpol clusters we used in the last chapter, we downweighed the massive clusters to take the SZ variance into account. This didn't have much effect on the final analysis as we had only few massive clusters. However, with future low noise CMB surveys such as SPT-3G, CMB-S4, Simons Observatory etc., downweighing won't be an optimal solution. The chapter is organised as follows: in §4.1 we describe the template fitting approach which will significantly reduce SZ variance, followed by results in §???. We forecast mass uncertainties future experiments using our proposed method in section and then we finally conclude in section.

4.1 Method

In this section we give a brief review of modified Quadratic Estimator (mQE) (for more detailed explanation refer Chapter 4), followed by the refinements of mQE to reduce SZ variance.

Cosmic Microwave Background (CMB) has no power at galaxy cluster angular scales due to silk damping and hence can be approximated as a gradient on arc minute scales. Gravitational lensing of CMB by cluster induces a dipole kind of structure on the top of gradient. The correlation between the background gradient and lensing dipole is known as gradient approximation. The QE (?) exploits the gradient approximation to estimate the lensing convergence profile $\hat{\kappa}$. Gradient approximation doesn't hold for all Fourier modes, in fact it holds good for only those Fourier modes which are correlated by reconstruction. Specifically, the lensing convergence can be estimated from a weighted product of filtered versions of a gradient map $G(\hat{n})$ and small-scale lensing map $L(\hat{n})$:

$$\hat{\kappa}_{\ell} = -A_{\ell} \int d^2\hat{n} e^{-i\hat{n}\cdot\ell} \text{Re} \{ \nabla \cdot [G(\hat{n})L^*(\hat{n})] \}. \quad (4.1)$$

Here, $\hat{\mathbf{n}}$ is the pointing unit vector, ℓ is angular multipole, and A_l is a normalization factor.

While designed to pull out the lensing-induced correlations between large-scale and small-scale CMB anisotropy, the QE is also sensitive to correlations due to foreground emission. Of particular concern is the cluster's own SZ emission, which is typically an order of magnitude larger than lensing signal. Two ways have been discussed in literature to eliminate/reduce the SZ bias. One way is to exploit the multiple frequency dependence of SZ signal and use linear combination of different frequencies to remove SZ. While this method completely eliminates SZ bias, it significantly increases the statistical uncertainty due to the higher noise level of the combined map. Another way is to lower the characteristic scale of the low pass filter on the gradient map as shown in ?. Lowering the gradient cut results in separation of the modes present in gradient and small scale dipole map; hence reducing the unwanted correlation. However, a stronger low-pass filter obviously reduces the number of modes used to measure the gradient, and thus decreases the signal-to-noise.

On the other hand, the modified QE instead eliminates this bias without increasing the variance significantly by using an SZ-cleaned map for the large-scale gradient map. The large-scale gradient map is chosen because the CMB has much more power on large scales, so the noise penalty from SZ removal has minimal impact. Note that while multiple foregrounds can be removed in principle, in practice the focus has been on removing the SZ signal. This is simply because the SZ signal introduces the largest bias. With the SZ signal present in only one of the two maps, there is no SZ-induced correlation between the two maps and no net bias on the reconstruction of the lensing convergence.

However the SZ emission in the small scale lensing map does add noise to the lensing reconstruction. Since under self-similarity of the SZ flux, y , is expected to scale with cluster mass M as $y \propto M^{5/3}$ while the lensing signal is linear in mass, the additional SZ variance will generally be more important for high-mass clusters. The SZ variance will also be more important in low-noise surveys, i.e. when it is larger than the instrumental noise in the convergence map.

4.1.1 *Template fitting to reduce the SZ variance*

As mentioned earlier, an obvious way to eliminate this SZ variance is by using SZ-free maps for both the small-scale and gradient maps. Of course this would undo the advantages of the modified QE for the instrumental noise in the small scale map. One can also reduce this extra variance by projecting out a model template for the SZ signal, and thereby reducing the total amount of SZ power in the small-scale map.

Template fitting has been considered previously in the context of the original QE (?). However, in that setting, residual SZ signals would bias the lensing masses. Even

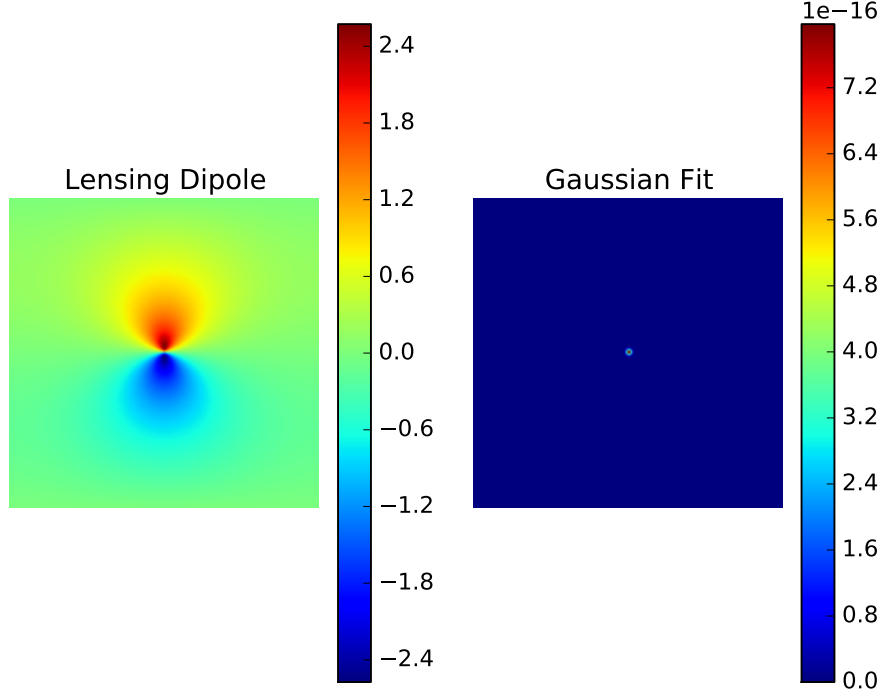


Figure 4.1: explain why no bias

one percent of residual SZ signal would lead to bias of six percent in mass estimation. This is not a problem in modified QE with SZ-free gradient map the residual SZ in the second leg won't introduce any bias.

To be unbiased, the template must not couple (on average) to the CMB lensing signal. This can be achieved by either fitting the template to a Compton y-map (i.e. using the different spectral dependence of the SZ and CMB to eliminate the CMB), or by using a template that has no average correlation with the lensing dipole pattern. The latter can be achieved by a radially symmetric template, fixed at the cluster position. To illustrate this we constructed a plane temperature gradient field and lensed it with galaxy cluster of mass $M_{200m} = 5 \times 10^{14} M_{\odot}$. We fit a radially symmetric Gaussian profile to the lensing dipole signal as shown in Fig. 4.1. The left panel in Fig. 4.1 is the lensing dipole signal and right panel is the best fit Gaussian profile. As can be seen the amplitude of the resultant Gaussian fit is of the order of 10^{-15} .

If the position is freed, the template can shift to pick up the negative lobe of the lensing dipole signal resulting in a low bias. Given the impossibility in creating a 'perfect' SZ template, the template fitting will not completely eliminate the SZ signal in the small-scale map. However, template fitting can significantly reduce the SZ power

in the small-scale map, and thus reduce the SZ noise penalty on the lensing mass reconstruction.

In this work, we take the tact of fitting a radially symmetric template at the fixed cluster location. Unless otherwise noted, we assume the beam to be a Gaussian with $\text{FWHM} = 1'$ at 150 GHz and $1'.7$ at 90 GHz. As this beam size is significant compared to the actual size of clusters at $z > 0.3$, clusters are approaching the effective point source limit where the specific details of their shape would not matter. Thus we choose to use a simple Gaussian template as the baseline template in this work. We also compare the results to template fitting with more physically motivated Arnaud profile (?), convolved by the experimental Gaussian beam. The residuals of removing a $2'.0$ FWHM Gaussian from an Arnaud profile convolved by a $1'.7$ beam are illustrated in Fig. 4.2. As argued above, the Gaussian significantly reduces the SZ signal despite the mismatch between the assumed profile and input SZ model. While there should be small variations in the typical size of the cluster's SZ emission with mass and redshift, we neglect these variations and fix the size of the templates based on the expected median mass and redshift of the sample.

Since the template will be applied to that small-scale map that has been high pass filtered at $\ell > 2000$, we apply a matching high pass filter to the map used for fitting and the SZ model template. This high-pass filter step is done in cutouts of $100' \times 100'$; we then pull out a central $10' \times 10'$ cutout at the cluster location for fitting the template. Since both the SZ emission and lensing signal extraction is concentrated within a few arcminutes of the cluster center, there is little reason to fit over a larger area. We allow for two free parameters in the fitting: the overall amplitude of the template, and a constant DC offset. Note that given the high-pass filter, we expect (and find) the DC term to be effectively zero. In any case, while we fit for a DC term when normalizing the template, we do not then remove the DC term. Only the template is subtracted from the small-scale map.

With template fitting included, the Fourier transforms of the two maps used by the quadratic estimator can be written down as:

$$G_\ell = i\ell W_\ell^G T_\ell^{\text{SZ-free}} \quad (4.2)$$

$$L_\ell = W_\ell^L (T_\ell - T_\ell^{\text{SZ-template}}) \quad (4.3)$$

where, G_ℓ is the large-scale gradient map and L_ℓ is the small-scale map. W_ℓ^G and W_ℓ^L are the Wiener filters to maximize the lensing signal ?. The mm-wave map is T_ℓ while the constructed SZ-free map is $T_\ell^{\text{SZ-free}}$. Compared to the modified QE (??), the new element is the $T_\ell^{\text{SZ-template}}$ term representing the SZ template fit.

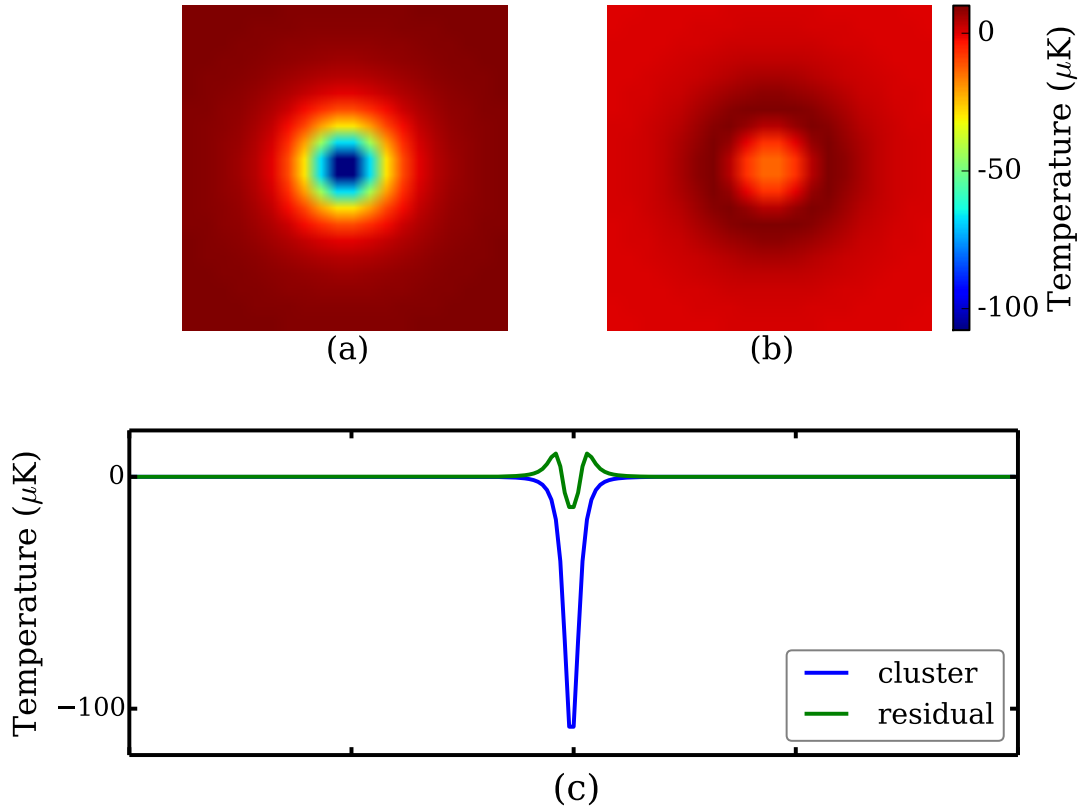


Figure 4.2: Template fitting significantly reduces SZ power, even with an imperfect match between the template and true SZ signal. The top left panel (a) shows the expected Arnaud profile for a galaxy cluster of mass $M_{200m} = 510^{14} M_{\odot}$ at $z=0.7$ after being smoothed by Gaussian beam with FWHM= $1'.7$. The top right panel (b) shows the residuals after subtracting the best-fit $2'.0$ FWHM Gaussian (the amplitude is free, but the FWHM is fixed). The lower panel (c) shows one-dimensional slices through each panel: the solid, blue line is a slice through the beam-convolved Arnaud profile of (a), and the dashed green line is a slice through the residual map in (b).

4.2 Results

4.2.1 Sources of uncertainty in the CMB-Cluster Lensing Measurement

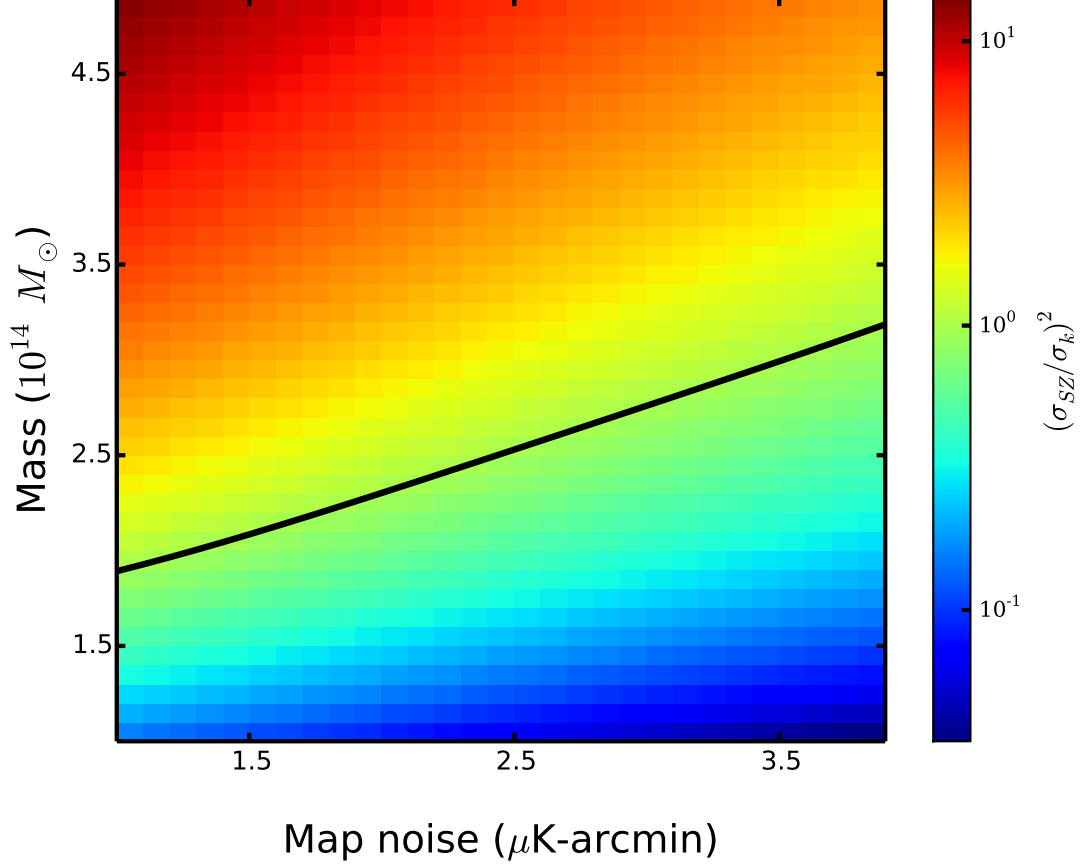


Figure 4.3: Ratio of SZ variance over kappa variance as a function of cluster mass and experimental noise level. As expected the ratio increases with mass for a given experimental noise level. The black solid line represents the points where the ratio SZ variance is equal to that of experimental noise.

Template fitting is intended to reduce the SZ variance, however it will do nothing for other sources of uncertainty such as instrumental noise, CMB sample variance and foreground emission (if not cleaned). Thus it will be useful to look at the relative magnitudes of these two terms, the SZ variance (σ_{SZ}^2) and the non-SZ variance (σ_{κ}^2), when interpreting the performance of template fitting in the next section. The non-SZ variance, σ_{κ}^2 , depends on the survey parameters (i.e. instrumental noise, and the degree to which foregrounds are cleaned) but is independent of the cluster properties. We estimate σ_{κ}^2 following the approach in ?. Briefly, we generate simulated CMB skies and add instrumental noise. We do not include the cluster's SZ emission or gravitational

lensing signal since the goal is to estimate the other noise terms. We apply the lensing pipeline to the simulated skies to estimate the convergence maps. We fit the convergence map to determine a mass, and take the scatter in these inferred masses over 1000 simulations to be σ_κ . **think I've made this inaccurate. need to fix/explain better**

In contrast, the SZ variance should increase with cluster mass, M , roughly as $\sigma_{sz}^2 \propto M^{5/3}$, while being independent of the survey parameters. We estimate the SZ variance using the same suite as simulations, however now adding the cluster's SZ emission to the small-scale lensing map. We continue using an SZ-free map for other leg of the QE, the large-scale gradient map. As before, we estimate the convergence maps, fit for masses and take the scatter in these inferred masses to estimate $\sigma_{SZ}^2 + \sigma_\kappa^2$.

We present the ratio of the SZ to non-SZ variances, $\sigma_{SZ}^2/\sigma_\kappa^2$, as a function of survey noise level and cluster mass in Fig.4.3. As expected, the ratio increases with mass at any given noise level. The black solid curve represents a ratio of unity when the SZ variance equals the non-SZ variance. We expect template fitting to significantly improve the mass uncertainties only for clusters above the black curve.

4.3 Results

As shown in Fig. 4.4, we find that template fitting leads to a significant improvement in the final mass uncertainties for CMB-cluster lensing. For high-mass clusters, template fitting does nearly as well as in the idealized (non-physical) limit of having no SZ emission. In this figure, we are assuming an SPT-3G like experiment with FWHM=1' at 150 GHz and a survey noise level of $3\mu\text{K-arcmin}$. We compare four algorithms to estimate cluster masses. First, the red solid line shows the performance of the original modified QE without template fitting. This uses an SZ-free gradient map (from a linear combination of 95 and 150 GHz maps) and use a 150 GHz map with SZ emission for the two legs of the QE. The second, black dotted line shows the results for an idealized case, where we again use an SZ-free gradient map but use a 150 GHz map without SZ for the small-scale map. Obviously the latter assumption is unphysical since there will be SZ emission at 150 GHz, but it shows the limit for how well perfect SZ subtraction might perform. Note that the relative performance improvement between the idealized and baseline cases increases with mass as expected. For these survey parameters, the idealized case has 17% smaller uncertainties than the baseline for clusters of mass $1 \times 10^{14} M_\odot$ and 50% smaller for cluster masses of $5 \times 10^{14} M_\odot$. Template fitting recovers nearly all of this gain for high-mass clusters.

modified QE uncertainties

(leaving out SZ)

for the gradient map and using

no SZ in the small-scale map of the QE. (2) using an SZ-free map only for the gradient leg of the QE, i.e. the modified QE, and (3) improved version of the modified

QE presented in this work, with an SZ-free map used for the gradient leg of the QE and projecting an SZ template out of the HPF leg.

4.3.1 *Performance comparison*

Here we compare three algorithms to estimate cluster masses: (1) using an SZ-free map in the gradient leg and no SZ in the HPF leg of quadratic estimator (2) using an SZ-free map only for the gradient leg of the QE, i.e. the modified QE, and (3) improved version of the modified QE presented in this work, with an SZ-free map used for the gradient leg of the QE and projecting an SZ template out of the HPF leg.

The performance of the three algorithms are shown in Fig. 4.4 as a function of cluster mass for an SPT-3G like experiment. All the curves show the percentage mass uncertainty for a sample 1000 clusters. Black curve represents an ideal case - SZ free gradient and no SZ in the second leg. Though not realistic, it gives lower bound we can achieve with template fitting. On the other hand, red curve gives the upper bound with SZ-free gradient and Arnaud SZ profile in the second leg. Blue and green curves show the improvement that can be achieved using our new method. For the blue and green curves, SZ signal present in the second leg is reduced by using Gaussian and Arnaud templates respectively.

As can be seen, both Arnaud and Gaussian template fitting perform equally well. This is unsurprising given that the angular size of the clusters is somewhat smaller than the instrumental beams; the beam-convolved signal is close to a Gaussian. While ideally template fitting approach should outperform modified QE at all mass scales, this is not the case in reality. At low cluster masses, experimental noise level dominates over SZ noise. In such cases the template fitting would be poor and our new approach achieves a minimal improvement over modified QE. On the other hand, at higher masses SZ variance is dominant source of uncertainty where the performance of our new method is considerable with the ideal case. **The improvement which we obtain over the modified QE depends on the mass of the cluster and the experimental noise level. While ideally template fitting approach should outperform modified QE at mass scales, this is not the case in reality.**

4.3.2 *Robustness of template fitting method*

As seen in the Fig. 4.4 our refinement for modified QE improves the fractional mass uncertainties significantly for all the masses considered. However, the realistic SZ may not be a radially symmetric as Arnaud profile predicts. So, in order to check the robustness of our new method we used realistic SZ simulations from Sehgal et al ? and Takahashi et al ?, the results of which are show in Fig. 4.6. We have only considered Gaussian fitting for the realistic simulations as there is no difference in the performance of both templates. The red and black curves in the figure are the results of modified QE for

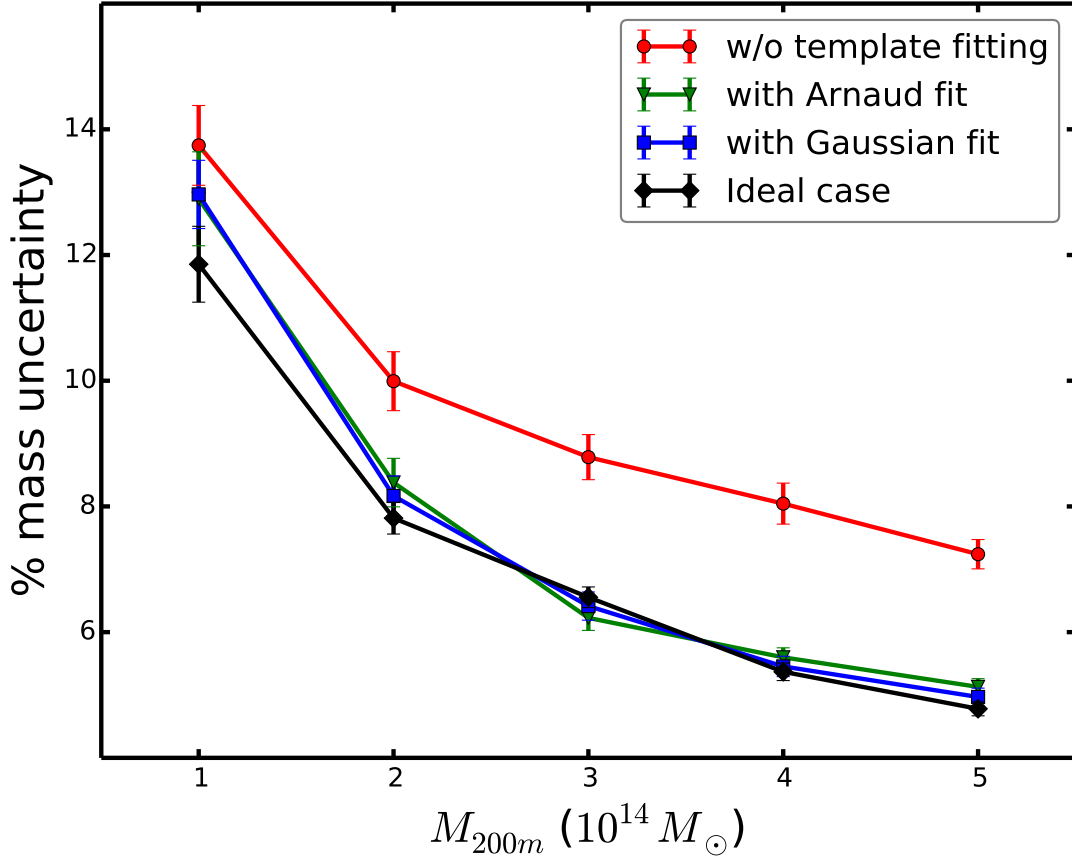


Figure 4.4: Projecting out an SZ template from the second leg of the modified QE improves the performance for all masses considered. Here we show the percentage mass uncertainties from three methods for a sample of 1000 clusters at an experimental noise level of $3 \mu\text{K-arcmin}$. All the curves use an SZ-free map for the gradient, but make different assumptions about the second, high-pass filtered map. [SR: Replace “mQE” to w/o template fitting. They are all mQE. Change xlabel to M_{200m} . Change line styles to match text].

Sehgal and Daisuke sims and the corresponding dashed curves show the improvements we obtain after subtracting Gaussian template from the second leg of modified QE. The apparent flattening of the red curve is due to the limited sample variance of Sehgal simulation at higher masses.

4.3.3 Miscentering

Previous works have found a positional offset of $0.5'$ between the SZ and X-ray centroid (?) or location of the brightest central galaxy (BCG)(?). Template fitting methods provides optimal results if cluster center is the SZ center. While this is not a problem for SZ selected clusters as both cluster and SZ center coincide, however, this may be a concern for clusters selected via X-ray or optical surveys. In such cases our new method will be optimal if we have additional fitting parameters for positional offsets. It

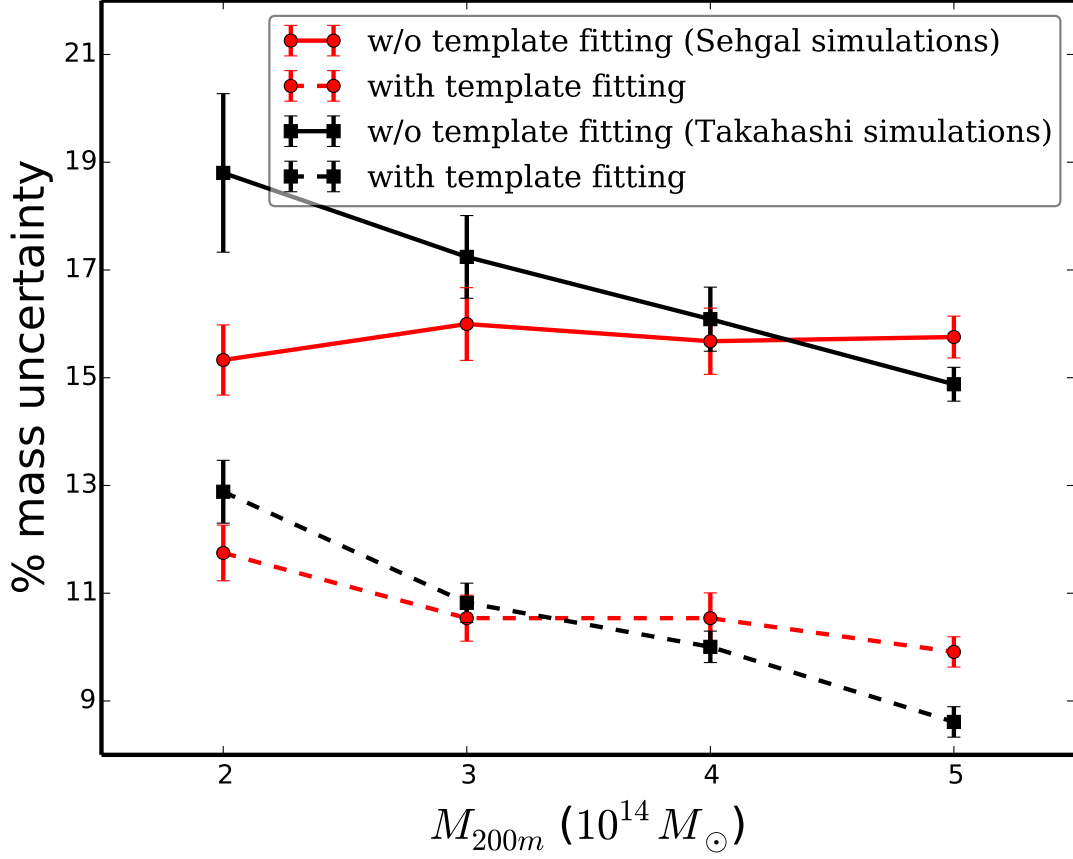


Figure 4.5: Our new method is robust to realistic SZ simulations. The red and black solid curves show the performance of modified QE for the Sehgal and Takahashi simulations respectively. The dashed lines show the improvement in each case when template fitting is used to reduce the SZ variance in the small-scale map. [SR: Change xlabel to M_{200m}].

is important to note that in such cases we can't use high pass filtered map as the lensing induced "dipole" present in the HPF map biases our fitting to lower masses. This bias can be removed by combining different frequency channels to remove CMB with slight decrement in SNR.

4.4 Forecasts

Now we predict the uncertainties expected on the stacked mass for the cluster samples from the CMB-S4 (?) and the Simons Observatory (SO)¹ (?) experiments. In both cases, we only consider the large-aperture telescopes (LAT) with an experimental beam of $\theta_{\text{FWHM}} = 1.4$ at 150 GHz and covering 40% of the sky (see also Table ??). We generated the expected cluster samples for the experiments without any foreground reduction technique using the 150 GHz channel. For this, using simulations we first

¹[SR: SO Goal: write more]

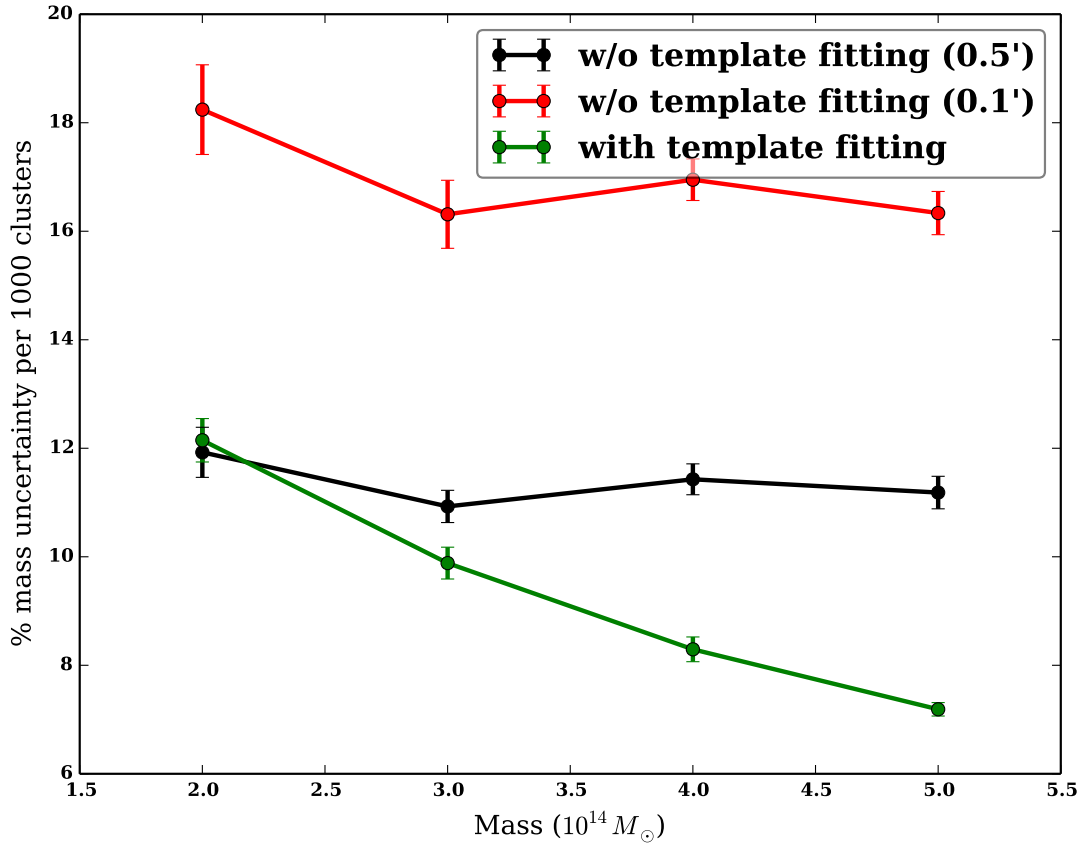


Figure 4.6: Our new method is robust to realistic SZ simulations. The red and black solid curves show the performance of modified QE for the Sehgal and Takahashi simulations respectively. The dashed lines show the improvement in each case when template fitting is used to reduce the SZ variance in the small-scale map. [SR: Change xlabel to M_{200m}].

estimate the detection significance S/N for clusters as a function of mass and redshift for the two experiments. The simulations contain signals from the primordial CMB, Gaussian foregrounds uncorrelated with the cluster, cluster tSZ emission modelled using Arnaud profile, and the respective white noise levels as given in Table ?? . The Gaussian foregrounds components were added using the measurements made by the SPT-SZ experiment (?) and contain emissions from radio, dusty galaxies, and the SZ signals from the low mass haloes that were unresolved by the SPT-SZ experiment. Next, we use the publicly available Halo Mass Function calculator (?) to obtain the halo counts ($dN/dz/d\log M$) per unit redshift ($\Delta z = 0.1$) and mass ($\Delta M = xx$) bin. Using the SNR look-up table from the above simulations, we get the number of clusters that will be detected above $S/N \geq 5$ by both the experiments. We estimate that CMB-S4 (SO) will detect approximately 75,000 (27,000) clusters. More details about the software used to generate the cluster sample will be given in a future work. We feed these cluster

samples into our lensing pipeline and predict the uncertainty in the stacked mass for the two samples. The results are given in Table ??.

We find ... w/o tSZ removal and xx after tSZ removal .. bit about SO and S4 including configuration and improvements obtained

Appendix A

Appendix A

A.1 Section in an appendix

This is an appendix chapter.